Differences between tangential geostrophy and columnar flow

Hagay Amit, Maria Alexandra Pais

To cite this version:

Hagay Amit, Maria Alexandra Pais. Differences between tangential geostrophy and columnar flow. Geophysical Journal International, 2013, 194 (1), pp.145-157. ⟨10.1093/gji/ggt077⟩. ⟨hal-02363379⟩

HAL Id: hal-02363379
https://hal.science/hal-02363379v1

Submitted on 19 Oct 2021

Geophysical Journal International

Geophys. J. Int. (2013) **194,** 145–157
Advance Access publication 2013 April 5

doi: 10.1093/gji/ggt077

Differences between tangential geostrophy and columnar flow

Hagay Amit[1] and Maria Alexandra Pais[2]

[1] *CNRS UMR* 6112, *Université de Nantes, Laboratoire de Planétologie et de Géodynamique,* 2 *rue de la Houssinière, Nantes, F*-44000, *France.*
E-mail: hagay.amit@univ-nantes.fr
[2] *CGUC, Physics Department, University of Coimbra,* 3004-516 *Coimbra, Portugal*

Accepted 2013 February 22. Received 2012 February 21; in original form 2012 October 10

SUMMARY

Core flows inverted from time-dependent geomagnetic field models image the geodynamo at the top of its generation region, the Earth's outer core. Physical assumptions incorporated in these inversions affect the resulting flows. Based on rapid rotation dominance, two assumptions similar in form yet different in essence have been proposed: tangential geostrophy (TG, LeMouël 1984) and columnar flow (CF, Amit & Olson 2004). We recall that CF is theoretically consistent with the quasi-geostrophy (QG) theory for an incompressible fluid with spherical solid boundaries whereas TG is not. As such, we highlight the importance of applying the CF assumption when inverting geomagnetic data for interior core (columnar) flows that can be used in kinematic dynamo and thermal convection models in the Boussinesq approximation. Next we evaluate the non-uniqueness associated with CF flows. The areas of ambiguous patches at the core surface where invisible TG or CF flows reside are roughly comparable. The spatial distribution of ambiguous patches for both TG and CF is quite asymmetric about the equator, so assuming equatorial symmetry is expected to reduce the non-uniqueness significantly. In fact, for assumed equatorial symmetry, the only possible non-unique flows will be those along hypothetical ζ-contours in the opposite hemispheres that their equatorial plane projections are parallel. TG flows exhibit a strong Atlantic/Pacific hemispheric dichotomy and a well-defined eccentric gyre whereas in CF flows the dichotomy between these two hemispheres is weaker and the gyre is less clear suggesting that the eccentric gyre might not conserve mass. Both TG and CF upwelling/downwelling patterns are strongly localized in the equatorial region. In addition, in both cases upwelling/downwelling is correlated with equatorward/poleward flow respectively, as expected for QG convection. CF upwelling is more intense than TG upwelling but the magnitude ratio is smaller than the factor 2 distinguishing the analytical expressions of the two assumptions. This smaller magnitude ratio is due to the fact that presently observed geomagnetic secular variation features are mostly explained by magnetic field advection by toroidal core flow in the frozen-flux approximation. Robust upwelling features below India/Indonesia may be viewed as geomagnetic evidence for whole core convection.

Key words: Inverse theory; Dynamo: theories and simulations; Geomagnetic induction; Rapid time variations; Satellite magnetics.

1 INTRODUCTION

The geomagnetic field is generated by the motion of an electrically conductive fluid in Earth's liquid metallic outer core in a process known as the geodynamo. Since 2000, the availability of high-quality geomagnetic field observations from both satellites and surface observatories has provided geomagnetic field and secular variation (SV) models of unprecedented reliability (Olsen & Mandea 2008; Lesur *et al.* 2010; Olsen *et al.* 2010; Finlay *et al.* 2012). Models of the radial geomagnetic field and its SV on the core–mantle boundary (CMB) have been used to infer the tangential fluid flow at the top of the core. These core flow models image the kinematics at the top of the core and may provide important dynamical insights into the working of the geodynamo. However, core flow inversions suffer from various problems that reduce their robustness (for reviews see Holme 2007; Finlay *et al.* 2010). Perhaps most notably, the inherent non-uniqueness in the inverse problem (Backus 1968) requires an additional hypothesis to be made about the flow, typically based on analytically derived or experimentally observed physical results. Different assumptions have been employed, including purely toroidal flow (Whaler 1980), steady flow (Gubbins 1982), tangential geostrophy (Hills 1979; LeMouël 1984), steady flow in a drifting reference frame (Holme & Whaler 2001), helical flow and columnar flow (Amit & Olson 2004) and tangential magnetostrophy (Asari & Lesur 2011). From hereafter we refer to tangential geostrophy as TG and to columnar flow as CF. The most popular assumption is TG (e.g. Gire & LeMouël 1990; Jackson 1997; Pais & Hulot 2000; Hulot *et al.* 2002; Eymin & Hulot 2005; Asari *et al.* 2009), primarily because it is consistent with the prevailing force balance in the limit of rapidly rotating flows. In addition, TG flows were found to be capable of reproducing the time variability required to explain the observed variations in the length of day (Jault *et al.* 1988; Jackson *et al.* 1993). Unlike purely toroidal flows, TG flows allow for convective (poloidal) motions relating the CMB with the deeper core. Finally, the TG assumption reduces (though does not eliminate) the non-uniqueness in the flow inversion. The extent at which TG reduces the non-uniqueness depends on the magnetic field morphology (Backus & LeMouël 1986; Chulliat & Hulot 2001; Chulliat 2004).

More recently, the quasi-geostrophy (from hereafter QG) approximation was invoked in the context of core flow inversions (Pais & Jault 2008; Gillet *et al.* 2009). These studies imposed equatorial symmetry outside the tangent cylinder and no flow crossing its rim. In addition to inferring the motions at the top of the core, these studies aimed to provide an understanding into the dynamics of the interior of the outer core (Gillet *et al.* 2010) and to hindcast/forecast the field via a data assimilation scheme (Canet *et al.* 2009). As these studies extend surface flows downwards to the core interior using the axial invariance assumption of the QG model, it is of great importance to use in the core flow inversion process physical assumptions that are consistent with QG. In this paper we stress that CF, rather than TG, is consistent with QG, as long as flow incompressibility is maintained.

The latter point deserves some attention. In our revision of the theory we will show that incompressibility is assumed in the derivation of the Taylor–Proudman constraint, that is, the invariance of the flow in the direction z of the rotation axis. This constraint is the basis for QG and CF. In addition, incompressibility just below the CMB is assumed in the derivation of CF. It therefore seems adequate to require that conservation of mass will be respected in conjunction with QG and CF. However, standard QG does not fully satisfy incompressibility. For a similar reason, TG columnar flows, derived from a compressible QG model, do not conserve mass. We will emphasize that a modified QG model as proposed by Schaeffer & Cardin (2005) in conjunction with the surface condition CF consistently enforce conservation of mass in both the volume and surface flows, in the framework of a QG approximation.

The amount and distribution of stretching of radial magnetic field by QG columns is important in studies that address the ability of QG flows to sustain the geodynamo (e.g. Schaeffer & Cardin 2006). In addition, the existence of upwelling near the CMB is currently under debate. Seismic studies (Helffrich & Kaneshima 2010) and estimates of large core thermal and electrical conductivities (Pozzo *et al.* 2012) may indicate that the top of the core is stably stratified. Our study highlights robust upwelling features which could be considered as geomagnetic evidence for whole core convection.

In this paper we compare the tangential geostrophy and columnar flow assumptions in terms of their theoretical consistency with quasi-geostrophy, their respective spatial distributions of non-unique regions, and the morphology of inverted core flows. In Section 2, we outline the theoretical background associated with these two assumptions. The core flow inversion method is described in Section 3. In Section 4, we use time-varying geomagnetic field models derived from recent satellite data and from the historical record to compare the patterns of non-uniqueness associated with each assumption and the respective inverted core flows. Theoretical and practical differences between the two assumptions are discussed in Section 5. Finally we summarize our main conclusions in Section 6.

2 THEORY

Core flow inversions solve the radial magnetic induction equation at the top of the free stream just below the CMB where the radial velocity vanishes. Assuming that magnetic diffusion is negligible (Roberts & Scott 1965), this equation yields

$$\frac{\partial B_{\mathrm{r}}}{\partial t} + (\vec{u}_{\mathrm{h}} \cdot \nabla_{\mathrm{h}}) B_{\mathrm{r}} + B_{\mathrm{r}} \nabla_{\mathrm{h}} \cdot \vec{u}_{\mathrm{h}} = 0, \tag{1}$$

where B_{r} is the radial magnetic field at the CMB, t is time, the subscript h denotes the direction tangent to spherical surfaces and $\vec{u}_{\mathrm{h}}$ is the tangential flow. The first term in (1) is the SV, the second term represents magnetic field advection by the flow and the third term denotes stretching/contraction of magnetic field by upwelling/downwelling. For given models of the radial field and its SV, eq. (1) may be viewed as one scalar equation with two scalar variables—the two tangential flow components u_ϕ (west–east) and u_θ (north–south) or alternatively the two flow potentials (toroidal and poloidal) (Holme 2007). This outlines an intrinsic non-uniqueness. Furthermore, a higher truncation degree in the spherical harmonics expansion is usually used for the flow than for the field scalar potentials, which increases the gap between the number of known SV coefficients to the number of flow coefficients to determine, resulting in a strongly underdetermined problem. An additional assumption is therefore needed to produce a better constrained flow solution.

The QG approximation applied to the volume flow and the TG and CF assumptions applied at the core surface, all stem from considerations on the dynamics in the core. The Navier–Stokes equation describes the magnetohydrodynamic force balance

$$\rho \frac{\partial \vec{u}}{\partial t} + \rho \vec{u} \cdot \nabla \vec{u} + 2\rho\Omega \hat{z} \times \vec{u} = -\nabla P + \mu \nabla^2 \vec{u} + \alpha \rho g_0 T \hat{r} + \frac{1}{\mu_0} (\nabla \times \vec{B}) \times \vec{B}, \tag{2}$$

where ρ is the mean density of the outer core fluid, $\vec{u}$ is velocity, $\vec{B}$ is magnetic field, Ω is rotation rate, $\hat{z}$ is a unit vector in the direction of the rotation axis, P is pressure, μ is dynamic viscosity, α is thermal expansivity, g_0 is gravitational acceleration, T is temperature (or in general codensity), $\hat{r}$ is a unit vector in the radial direction and μ_0 is permeability of free space. The first two terms on the left-hand side of (2) are the inertial forces and the third term is the Coriolis force. The terms on the right-hand side of (2) are the pressure gradient, viscous, buoyancy and Lorentz forces, respectively. The flow must also obey a conservation of mass equation. The continuity equation represents conservation of mass in incompressible conditions

$$\nabla \cdot \vec{u} = 0 \quad . \tag{3}$$

At the spherical CMB surface, eq. (3) can be written as

$$\frac{\partial u_{\mathrm{r}}}{\partial r} = -\nabla_{\mathrm{h}} \cdot \vec{u}_{\mathrm{h}} \tag{4}$$

Two non-dimensional numbers often used to characterize the importance of rotational effects are the Ekman number $E = \nu/\Omega L^2$ representing the ratio of viscous to Coriolis forces (where $\nu = \mu/\rho$ is the kinematic viscosity), and the Rossby number $Ro = U/\Omega L$ representing the ratio of inertial to Coriolis forces, where U and L are typical velocity and length scales. For the Earth's core $\nu \sim 10^{-6}\,\mathrm{m}^2\ \mathrm{s}^{-1}$, $\Omega = 7.292 \times 10^{-5}\ \mathrm{s}^{-1}$, $L \sim 10^6$ m and

$U \sim 5 \times 10^{-4}\,\mathrm{m\,s^{-1}}$ (Finlay *et al.* 2010), giving $E \sim 10^{-14}$ and $Ro \sim 10^{-6}$. These extremely low values indicate that inertial and viscous forces are negligible with respect to the leading Coriolis force in (2). Thus to a leading order the dynamical balance in the Earth's core is expected to be among Coriolis, pressure, buoyancy and Lorentz forces, which is known as the magnetostrophic balance

$$2\Omega\hat{z} \times \vec{u} = -\frac{1}{\rho}\nabla P + \alpha g_0 T\hat{r} + \frac{1}{\rho\mu_0}(\nabla \times \vec{B}) \times \vec{B}. \qquad (5)$$

This is the starting point to the QG, TG and CF assumptions. We now recall in detail the specific derivation associated with each assumption.

2.1 Quasi-geostrophy

The geostrophic balance is obtained as a simplification of the Navier–Stokes equation in the entire outer core volume, when only the Coriolis and pressure forces contribute to determine the flow, to leading order

$$2\Omega\hat{z} \times \vec{u} = -\frac{1}{\rho}\nabla P. \qquad (6)$$

Taking the curl of (6) and assuming an incompressible flow (3) gives the Taylor–Proudman theorem

$$\frac{\partial\vec{u}}{\partial z} = 0, \qquad (7)$$

that is, the flow is invariant in the direction z parallel to the rotation axis.

The quasi-geostrophy approximation incorporates the z-invariance of the Taylor–Proudman constraint (7) for the component of the flow parallel to the equatorial plane but it additionally takes into account the non-parallel spherical solid boundaries of the container. It has arisen from efforts to understand the columnar structure of convecting flows in rapidly rotating spherical shells (Busse 1970), expected from theory (7) and observed in laboratory experiments (Busse & Carrigan 1976; Cardin & Olson 1994). The QG flow model is of the form

$$\vec{u} = \nabla \times (\psi(s,\phi,t)\hat{z}) + u_z(s,\phi,z,t)\hat{z}, \qquad (8)$$

where cylindrical coordinates (s, ϕ, z) are the most adequate due to the dominant symmetry imposed by rotation. The first term represents non-divergent motion denoted by the streamfunction ψ in the equatorial plane. The second term represents the axial flow that is needed to satisfy the non-penetration boundary condition. Note that while (8) perfectly satisfies the non-penetrating boundary conditions, it only approximately satisfies z-invariance (7) and incompressibility (3).

Assuming uniform axial variation of u_z in the liquid volume, $u_z \propto z$ and can be written as (Amit & Olson 2004)

$$u_z(s,\phi,z,t) = -\frac{sz}{H_c^2}u_s(s,\phi,t) = -\frac{z}{H_c^2}\frac{\partial\psi}{\partial\phi}(s,\phi,t) \qquad (9)$$

where $H_c = \sqrt{R^2 - s^2}$ is half the height of a column at distance s from the rotation axis. The model is completely defined by the streamfunction in the equatorial plane, ψ.

The axial flow u_z given by (9) was originally treated as a perturbation, associated with slight boundary slopes (e.g. Busse 1970). The fact that it introduces a violation of mass conservation was seen as a second order effect. In practice, the QG flow model is used even when the boundary slope is steep, leading to first order values for u_z and to compressibility effects, as can be seen from (8) where the first term on the right-hand side is divergent-free and cannot compensate for the axial mass displacement associated with the second term (see also 9). Because the QG model does not conserve mass, different results are obtained for $\partial u_r/\partial r$ and $-\nabla_h \cdot \vec{u}_h$ at the CMB.

Schaeffer & Cardin (2005) proposed a modified QG model which enforces mass conservation properly. They added to (8) an axial invariant azimuthal term, whose divergence cancels out the u_z divergence. Their modified incompressible QG flow model can be written as (see e.g. Pais & Jault 2008)

$$\vec{u} = \nabla \times (\xi(s,\phi,t)\hat{z}) + u_z(s,\phi,z,t)\hat{z} + \frac{s}{H_c^2}\xi(s,\phi,t)\hat{\phi} \qquad (10)$$

where ξ is termed a 'pseudo-streamfunction' (see also Pais & Jault 2008) and u_z is obtained from ξ according to (9), if we replace ψ by ξ. However, the azimuthal flow u_ϕ is obtained in a different way, from $u_\phi = -\partial\psi/\partial s$ with the standard QG model (8) and (9), to $u_\phi = -\partial\xi/\partial s + (s/H_c^2)\xi$ with the modified QG model.

2.2 Tangential geostrophy

The TG constraint is derived from the tangential component of the magnetostrophic balance equation at the top of the core, where the (radial) buoyancy force does not participate. Near the core surface the tangential components of the Lorentz force are assumed negligible (LeMouël 1984). The remaining balance between the tangential Coriolis and pressure gradient forces is termed tangential geostrophy and yields

$$2\Omega(\hat{z} \times \vec{u})_h = -\frac{1}{\rho}\nabla_h P \quad . \qquad (11)$$

It has the same expression as the geostrophy balance governing midlatitude synoptic-scale flows in the atmosphere and in the oceans (e.g. Pedlosky 1987). However, it differs from those cases in that it only applies at the core surface, whereas in the atmosphere and oceans the hydrostatic approximation is used for the vertical component of the momentum equation and the geostrophy balance determines the main horizontal flow inside the whole fluid shell. Note that (11) is not the 2-D version of (6), since it derives from a magnetostrophic 3-D force balance (5) at a particular spherical surface, the CMB.

Using the fact that the radial velocity vanishes on approach to the CMB, (11) becomes

$$2\Omega(\hat{r} \times \vec{u}_h)\cos\theta = -\frac{1}{\rho}\nabla_h P \qquad (12)$$

where θ is colatitude. Finally, the well-known TG constraint can be obtained by taking the divergence of the cross product of $\hat{r}$ with (12)

$$\nabla_h \cdot (\vec{u}_h\cos\theta) = 0 \qquad (13)$$

or

$$\nabla_h \cdot \vec{u}_h = \frac{\tan\theta}{R}u_\theta, \qquad (14)$$

where R is the core radius.

The TG assumption has also been derived in the context of the QG approximation. In this case, the dynamical support for TG is no longer tangential magnetostrophy with a negligible horizontal Lorentz force at the CMB (LeMouël 1984) but rather the dominance of Coriolis and pressure forces. Pais & Jault (2008) reconstructed the surface (u_θ, u_ϕ) flow using the QG model expressions (8) and (9) and showed that the resulting tangential divergence satisfies (13). This motivated the use of the TG assumption in the context of the

QG approximation, with equatorial symmetry additionally imposed (e.g. Pais & Jault 2008; Gillet *et al.* 2009). In a framework where we allow for deviations from divergence-free flows, the TG assumption can therefore be used to compute QG flows.

2.3 Columnar flow

The assumption termed columnar flow by Amit & Olson (2004) is merely the surface expression of QG in incompressible conditions. The dynamical support for CF is therefore the dominance of Coriolis and pressure forces. Amit & Olson (2004) showed (see their appendix) that rewriting (9) in spherical coordinates, differentiating by r and imposing incompressibility at the core surface (4), gives

$$\nabla_\mathrm{h} \cdot \vec{u}_\mathrm{h} = 2\frac{\tan\theta}{R} u_\theta \tag{15}$$

or

$$\nabla_\mathrm{h} \cdot \left(\vec{u}_\mathrm{h} \cos^2\theta\right) = 0. \tag{16}$$

Note that (15) differs from (14) only by a factor of 2. That the derivation of the CF upwelling gives a different expression (by a factor 2) than the TG expression is not a surprise, since as pointed out above the QG model defined by flow eqs (8) and (9) does not verify the incompressibility condition.

In words, the CF assumption stems from computing the upwelling at the CMB consistent with the relation between u_z and u_s as prescribed by the QG model and further imposing the incompressibility condition. For consistency, equatorial symmetry is further required, to guarantee that columns intercepting the CMB in the Northern Hemisphere are axially continued and connected to columns at the Southern Hemisphere.

In the framework of the modified QG model of Schaeffer & Cardin (2005), the CF derivation of the CMB upwelling is still valid because it does not depend on u_ϕ. Moreover, the CF assumption is fully consistent with the volume flow. In addition, the derivation of $\nabla_\mathrm{h} \cdot \vec{u}_\mathrm{h}$ as in Pais & Jault (2008) also yields the same result, given by (15). The agreement among these different derivations shows that the modified QG model in conjunction with the surface condition CF consistently enforce conservation of mass in both the volume and surface flows, in the framework of a QG approximation. This condition is important for proper downward projection of inverted surface core flows to the fluid core volume.

2.4 Ambiguous regions

Backus & LeMouël (1986) noted that a TG flow is non-unique (or partly invisible in terms of geomagnetic SV) along contours of $\zeta_\mathrm{tg} = B_\mathrm{r}/\cos\theta$ (see Appendix A). They further proved that due to the intersection of different ζ_tg contours at nodes where $B_\mathrm{r} = 0$ curves cross the geographical equator, the non-uniqueness is reduced to ambiguous regions bounded by ζ_tg contours that do not cross the equator (see also Chulliat & Hulot 2000).

CF is associated with a different geometry of non-unique regions. Eq. (16) implies non-uniqueness along contours of $\zeta_\mathrm{cf} = B_\mathrm{r}/\cos^2\theta$ (see again Appendix A). Since different ζ_cf contours intersect the geographical equator at nodes (just as ζ_tg), with CF the non-uniqueness is also reduced to ambiguous regions of the CMB bounded by contours of ζ_cf that do not cross the equator.

3 METHOD

Here, we describe our core flow inversion scheme and the different assumptions imposed on the four flow models. Writing the core surface flow in terms of the toroidal ($\mathcal{T}$) and poloidal ($\mathcal{P}$) scalar fields,

$$\vec{u}_\mathrm{h}(\theta, \phi) = R\nabla_\mathrm{h} \times (\mathcal{T}\hat{r}) + R\nabla_\mathrm{h}\mathcal{P}, \tag{17}$$

we use a regularized weighted least squares method to invert eq. (1) for a set of spherical harmonic coefficients of the two scalar potentials in (17), truncated to degree $\ell = 26$. In the inversion, we use the satellite data derived geomagnetic field model CHAOS-3 (Olsen *et al.* 2010) truncated to degree 13. The core flow estimations are expected to explain the model within a certain degree of confidence, which comprises both the information on the noise level of the SV 'data' with variance $\sigma^d(\ell)^2$ and an estimation of the SV signal produced by a non-parametrized contribution of the advection of main field small scales by the flow, $\sigma^r(\ell)^2$. The choice for these error models is the same as in Schaeffer & Pais (2011), namely $\sigma^d(\ell)^2 = 0.01(2\ell + 1)^{-1}(\ell + 1)^{-1}$ $(nT/yr)^2$ (Olsen *et al.* 2010) and $\sigma^r(\ell)^2 = 36 \exp^{-\ell}$ $(nT/yr)^2$ at the Earth's surface. The spatial resolution error model $\sigma^r(\ell)^2$ is intermediate to the two models used in Gillet *et al.* (2009) for the field models CM4 and xCHAOS and is also close to the models computed by Pais & Jault (2008). Common to all inversions is the ℓ^3 regularization term constraining small flow scales. It imposes a flow spectral decay consistent with the minimization of the sum of squares of tangential divergence and radial vorticity (Gillet *et al.* 2009).

As further physical assumptions, used to include the expected rapid rotation behaviour expressed by the QG model, conditions (13) and (16) are written in the spectral domain (see Pais & Jault 2008, for details) and introduced in the inversions as regularization terms associated with very high Lagrange multipliers. We invert for only $\ell + m$ odd toroidal and $\ell + m$ even poloidal coefficients, in order to obtain equatorially symmetric *TG-S* and *CF-S* flows, respectively. In contrast to Pais & Jault (2008), we do not impose a flow barrier at the latitude of the tangent cylinder in these equatorially symmetric flows.

The TG constraint can also be used in the context of a tangential magnetostrophic balance where the horizontal Lorentz force is neglected but the buoyancy force is kept, as explained in Section 2.2. In that case the thermal wind flow is not required to be equatorially symmetric. We computed for this case a *TG-AS* flow. Note that we have not applied the CF assumption without imposed equatorially symmetry because there is no theoretical support for such an inversion. Finally, because either TG or CF inhibit the flow from crossing the geographic equator and tend to focus tangential flow sources and sinks there, we also compute a fourth flow using only the ℓ^3 regularization, *N-AS*.

4 RESULTS

Here we present the results of our comparison between the TG and CF assumptions. We quantify the global non-uniqueness reduction associated with each assumption. Core flow models inverted using each assumption are compared. Two flow models assume equatorial symmetry with TG and CF, respectively, one model assumes TG without equatorial symmetry, and one model assumes only large-scale flow. The comparison among these four core flow models includes patterns and magnitudes, with special attention to the resulting upwelling distributions and amplitudes.

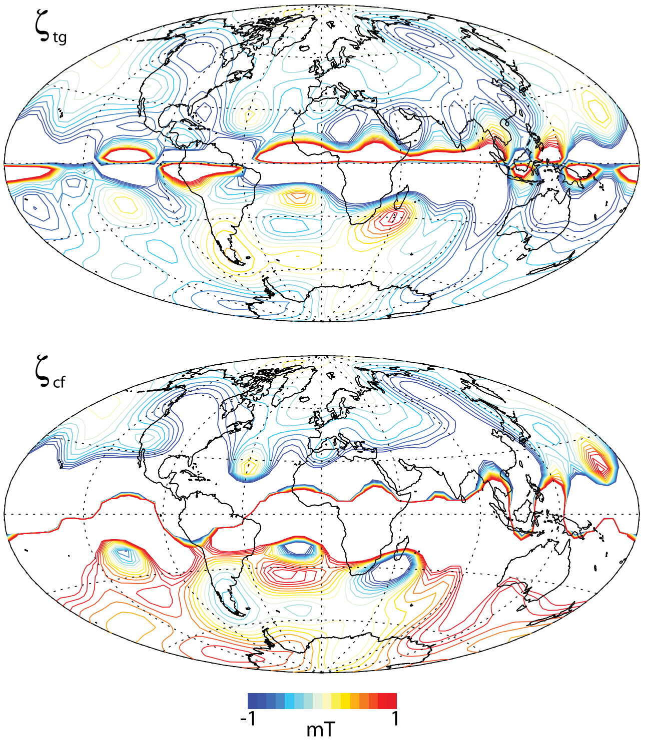

Figure 1. Contours of invisible flows ζ_{tg} (top) and ζ_{cf} (bottom) for the field model *gufm1* of Jackson *et al.* (2000) for the year 1980.

4.1 Non-uniqueness

We use the historical field model *gufm1* (Jackson *et al.* 2000) at 1980 to compare the non-uniqueness distributions associated with the TG and CF assumptions. The year 1980 was chosen as this was a particularly well magnetically monitored year thanks to the MAGSAT mission. The TG invisible flow contours $\zeta_{\mathrm{tg}} = B_{\mathrm{r}}/\cos\theta$ and the CF invisible flow contours $\zeta_{\mathrm{cf}} = B_{\mathrm{r}}/\cos^2\theta$ for this field model are plotted in Fig. 1. The scale is saturated at low latitudes due to the singularity at the equator. We set the saturation level to 1 mT, which was previously argued to be a reasonable threshold for an ageostrophic belt on the CMB (Chulliat & Hulot 2000). At low latitudes all ζ-contours converge to cross the geographical equator at points known as nodal points (Backus & LeMouël 1986). In the *gufm1* model for 1980, there are six equatorial nodal points. At higher latitudes some 'ambiguous islands' of closed ζ_{tg} and ζ_{cf} contours exist, where the flows are partly invisible.

The distributions of ambiguous regions are very similar for the TG and CF flows. Colour differences between the two plots, mostly in the Southern Hemisphere, are simply due to the different symmetries of $\cos\theta$ and $\cos^2\theta$ relative to the equator. There is no significant geometrical distortion and the difference lies essentially in a latitude-dependent amplification of ζ_{cf} values. In both ζ_{tg} and ζ_{cf}, ambiguous regions at mid- and high-latitudes tend to be non-symmetric with respect to the equator, especially below the south Atlantic.

To quantify the global non-uniqueness, we designed an algorithm to calculate the portions of CMB non-unique areas A_{tg} and A_{cf} associated with each of the two assumptions (see Appendix B). In this algorithm, a gridpoint on the core surface is counted as belonging to an ambiguous patch and contributes to A if it lies on a ζ curve that does not cross the geographic equator and closes on itself. Table 1 shows the relative areas of ambiguous patches for three snapshots from *gufm1* as well as one from the recent high-resolution high-quality geomagnetic field model *CHAOS-3* (Olsen *et al.* 2010) derived from satellite and surface observatory data. The time evolution of the computed areas is slow compared with the SV timescale, since it evolves with the main field. During the historical period, variations of up to ∼10 per cent may appear in the ambiguous patches areas. For a given field model and epoch, A_{tg} and A_{cf} are roughly comparable, with slightly lower values for CF flows in three of the four tested epochs. For the *CHAOS-3* field model of 2010, TG ambiguous patches cover 46.3 per cent of the CMB, while CF ambiguous patches cover only 41.3 per cent of the CMB. Snapshots from *gufm1* typically exhibit smaller differences between A_{tg} and A_{cf} (Table 1).

Table 1. Relative areas of ambiguous patches associated with tangential geostrophy A_{tg} and columnar flow A_{cf} for different field models. The corresponding quantities for equatorially symmetric ambiguous regions are denoted by a superscript 's'. All relative areas are given in per cent.

Field model	Year	A_{tg}	A_{cf}	A^{s}_{tg}	A^{s}_{cf}
CHAOS-3	2010	46.3	41.3	12.9	10.6
gufm1	1980	43.2	42.2	11.5	10.9
gufm1	1940	50.1	52.9	16.0	17.6
gufm1	1900	43.7	42.0	10.0	10.1

If the core flow is symmetric about the equator, then a pair of points (ϕ, θ) and $(\phi, \pi - \theta)$ is considered non-ambiguous if one of the points is ambiguous and the other is not. Following this rational, we define the 'symmetric portions' of CMB non-unique areas A^{s}_{tg} and A^{s}_{cf}. These symmetric areas cover only about 10–20 per cent of the CMB (Table 1), a much smaller area than A_{tg} or A_{cf}.

4.2 Core flows

Next we compare the TG and CF flows inverted from the geomagnetic *CHAOS-3* model. All flows are computed for each year over the period 1997–2010 covered by *CHAOS-3*, and then time-averaged. We show maps of contours of the toroidal flow potential $\mathcal{T}$ with, in colour-scale, the tangential divergence superimposed. Figs 2(a)–(b) show the *TG-S* and *CF-S* core flow models, respectively, both with imposed equatorial symmetry. To test the importance of imposing equatorial symmetry, we also compute a TG flow that is not forced to be symmetric about the equator (*TG-AS*, Fig. 2c). Finally, we test the effect of imposing kinematic conditions that forbid the flow to cross the equator and invert for a flow using the ℓ^3 norm as the only regularization (*N-AS*, Fig. 2d). All flows explain equally well the SV; that is, the normalized misfit is 1.0 for all inversions, taking into account the SV covariance error values that include both $\sigma^{d}(\ell)$ and $\sigma^{r}(\ell)$ as introduced in Section 3. In addition the TG and CF flows satisfy well their respective assumptions, with the CF assumption slightly better in *CF-S* than the TG assumption in *TG-S* and *TG-AS*, for the same Lagrange multiplier value. This is demonstrated through computation of σ^{p}_{cf} and σ^{p}_{tg} values that quantify the flow deviation from perfect CF and TG conditions, respectively, normalized by the flow deviation from purely toroidal (see smaller σ^{p}_{cf} than σ^{p}_{tg} in Table 2).

We find a large, well-delimited, eccentric gyre in the *TG-S* flow with clear Atlantic/Pacific hemispheric dichotomy in core flow activity. In contrast, in the *CF-S* flow the Pacific Hemisphere is somewhat more active. Azimuthal motions govern the *TG-S* flow under the low-latitude Atlantic Hemisphere whereas in the *CF-S* flow azimuthal motions extend below the Pacific.

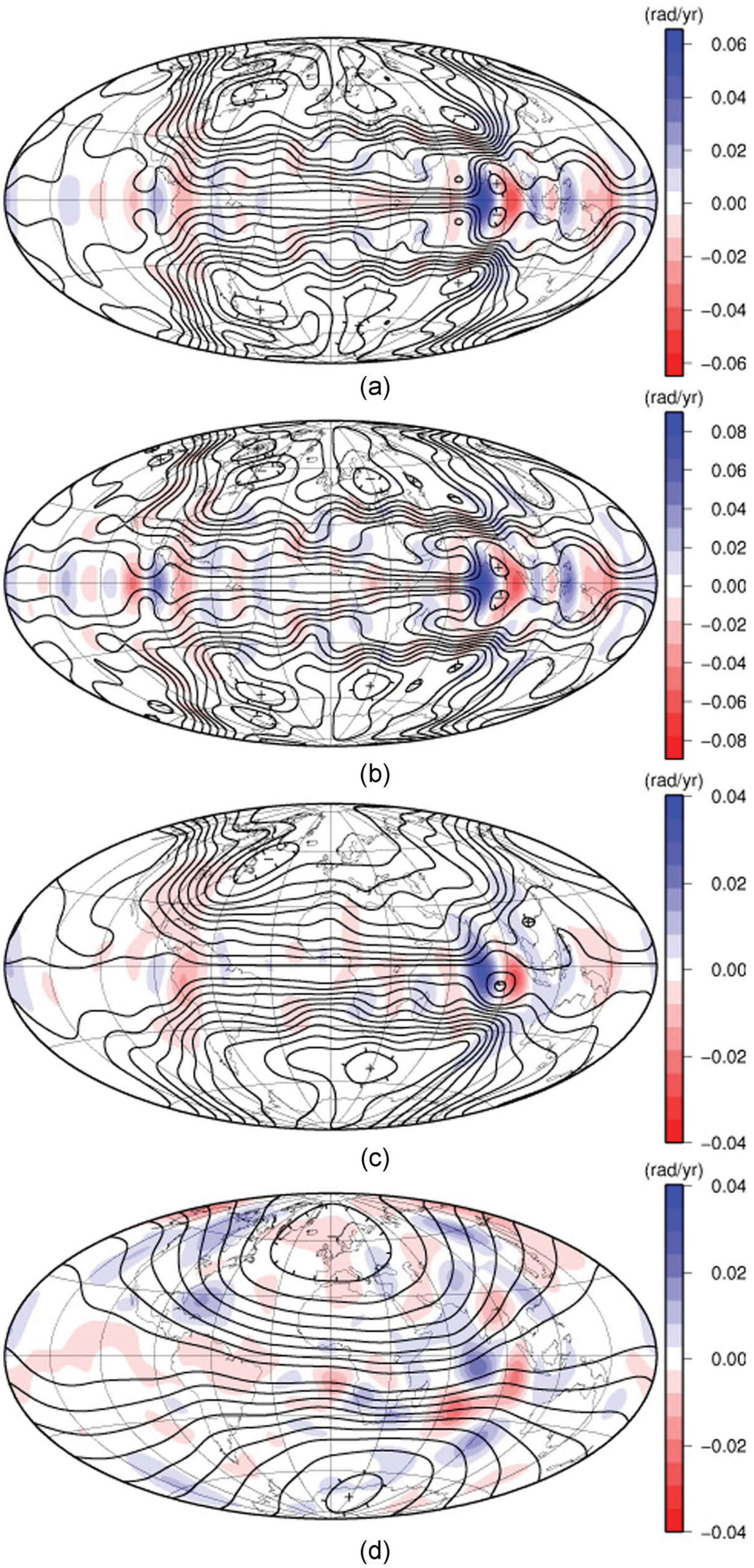

Figure 2. Time-average flows: Streamfunction (contours of the toroidal scalar) and upwelling (colour scale) based on inversions of the geomagnetic field and SV from the *CHAOS-3* model of Olsen *et al.* (2010) for the period 1997–2010. Plus/minus signs denote counter-clockwise/clockwise circulation, respectively, blue/red denote upwelling/downwelling, respectively. (a) Tangential geostrophy – symmetric, (b) columnar flow – symmetric, (c) tangential geostrophy – no symmetry imposed, (d) no assumption imposed.

Table 2. RMS (denoted by $\langle\rangle$) velocities and assumption misfit σ^p for different flows. The relative assumption misfit is defined for TG by $\sigma^p_{\mathrm{tg}} = \langle \nabla_{\mathrm{h}} \cdot (\vec{u}_{\mathrm{h}} \cos\theta)\rangle \,/\, \langle \nabla_{\mathrm{h}} \cdot \vec{u}_{\mathrm{h}}\rangle$ and for CF by $\sigma^p_{\mathrm{cf}} = \left\langle \nabla_{\mathrm{h}} \cdot \left(\vec{u}_{\mathrm{h}} \cos^2\theta\right)\right\rangle \,/\, \langle \nabla_{\mathrm{h}} \cdot \vec{u}_{\mathrm{h}}\rangle$. All flows are time-averages for the period 1997–2010, computed using inversions of the *CHAOS-3* geomagnetic field model of Olsen *et al.* (2010). RMS values are given in km yr^{-1}.

Flow model	$\langle \vec{u}_{\mathrm{tor}} \rangle$	$\langle \vec{u}_{\mathrm{pol}} \rangle$	$\langle \vec{u} \rangle$	σ^p
TG-S	13.6	3.1	14.0	1.4×10^{-8}
CF-S	13.7	4.2	14.4	7.0×10^{-9}
TG-AS	11.0	2.6	11.3	4.1×10^{-8}
N-AS	7.5	2.3	7.8	–

When using fewer constraints for the flow inversion while still keeping the same SV fit criterion, the remaining constraints are given more weight. Accordingly the large scale flow constraint becomes more evident when the equatorially symmetric condition is removed to compute the *TG-AS* flow, and at a greater degree when we further remove the TG constraint to compute the *N-AS* flow. The single ℓ^3 regularization in the *N-AS* case results in a very large scale flow, which fits the SV model as closely as the other three flows.

By far the most intense upwelling/downwelling structures for *TG-S* and *CF-S* flows emerge right at the equator below South America and mainly under the India/Indonesia region at the limbs of the large eccentric gyre where the flow is meridional. Poleward/equatorward flow is correlated with downwelling/upwelling, respectively. The upwelling patterns of the *TG-S* and *CF-S* flows are similar, with a larger amplitude in the latter. A similar upwelling pattern but somewhat larger scale and weaker is found in the *TG-AS* case. In the *N-AS* case the upwelling pattern is no longer confined to the equator but is well distributed over the CMB.

Table 2 compares the magnitudes of the four flows. The toroidal component is dominant in all cases. The magnitudes of the *TG-S* and *CF-S* flows are similar. The toroidal components of these flows are also similar, but the poloidal component of the latter is about 30 per cent larger. This increase is expected from the imposed increase in the tangential divergence, although a much larger increase of 100 per cent may have been expected (compare 14 and 15). We explain the reason for the smaller than 2 ratio in the Discussion. Decreasing the number of constraints on the flow increases the relative importance of the remaining constraints. As a result, the *TG-AS* flow that was computed by removing the equatorially symmetric condition is less energetic than the equatorially symmetric *TG-S* flow while dropping the TG constraint produces the even less energetic *N-AS* flow.

The contributions of magnetic field advection and stretching to the SV are shown for each flow model in Fig. 3. The SV is mainly explained by the advection term in most of the CMB. Comparison between the advection and stretching contributions to the SV in the *TG-S* (Fig. 3b) and *CF-S* (Fig. 3c) flows shows that the stretching term is only moderately larger in *CF-S*, as can be seen at the equatorial region below India and Indonesia.

To further characterize the different flows we show the zonal profiles $\overline{u}_\phi(\theta) = (1/2\pi)\int u_\phi \mathrm{d}\phi$ and $\sqrt{\overline{u^2_\theta}}(\theta) = \sqrt{(1/2\pi)\int u^2_\theta \mathrm{d}\phi}$ (note that $\bar{u}_\theta$ would be 0 for TG and CF flows because of null zonal poloidal coefficients) in Fig. 4. The strong westward jet near the tangent cylinder is clearly seen in the *TG-S* and *CF-S* flows, as well as the westward jets at latitudes 30° and at the equator. Comparing *TG-S* and *CF-S* flows, the requirement of mass conservation causes $\sqrt{\overline{u^2_\theta}}$ to decrease and $\bar{u}_\phi$ to increase at mid- and low-latitudes of *CF-S*, suggesting a zonation or spiralling of the flow. Relaxing the equatorial symmetry constraint in *TG-AS* and *N-AS* reveals north–south asymmetry. The high-latitude westward jet is stronger in the Northern Hemisphere whereas the westward jet at low- and mid-latitudes is much stronger in the Southern Hemisphere. The increasing effect of regularization in *TG-AS* and *AS-N* flows is seen both in $\sqrt{\overline{u^2_\theta}}$ and $\overline{u}_\phi$, with a decrease in RMS flow magnitudes. Note that the tangent cylinder is crossed by the flow as evident by the non-negligible $\sqrt{\overline{u^2_\theta}}$ values at related colatitudes. The purely azimuthal flow at the equator, characteristic of *TG* (*-S* or *-AS*) and *CF-S* flows, is clearly outlined.

5 DISCUSSION

Recent work on inversion of geomagnetic field models for core surface flows in the framework of a QG approximation have used either TG or CF assumptions, together with imposed equatorial symmetry (Pais & Jault 2008; Gillet *et al.* 2009; Schaeffer & Pais 2011). In this study, we revise the theoretical arguments in favour of each assumption. We derive for the first time the non-uniqueness distribution associated with CF and compare it with that associated with TG. We then examine closely ensuing differences in the computed TG and CF core flows, which has never been done so far.

5.1 Theoretical consistency with QG and incompressibility

The compliance (or lack thereof) of inverted flows with the divergence-free flow condition (3) and its surface expression at the CMB (4) is a main aspect to distinguish equatorially symmetric TG from CF flows. This is not a minor point, if these flows are to be downward projected into the core interior and used in kinematic dynamo and thermal convection models. Most core dynamics models solve for a divergent-free flow. Density perturbations are treated in the framework of the Boussinesq approximation, which is a reasonable approach given that density probably changes by only about 20 per cent in the liquid core (e.g. Christensen & Wicht 2007). The poloidal/toroidal decomposition commonly used for the flow in these situations requires by construction a divergent-free flow. Blindly projecting the columnar flow inferred from core surface models onto a poloidal/toroidal basis will cause losing a flow component in case of columnar TG flows, a component which was in principle constrained by geomagnetic data.

Another theoretical issue concerns the computation of equatorially symmetric TG flows using the radial magnetic induction equation. Is this equation compatible with deviations from incompressibility in the symmetric TG flows as reported above? The divergence-free flow condition (3) is usually used to derive the radial magnetic induction equation at the CMB, and it could seem inconsistent, at first sight, to use this equation to invert for a compressible flow. However, the radial component of the induction eq. (1) can also be derived in the frozen-flux approximation without imposing flow incompressibility. The third term in (1) may have different physical interpretations. For an incompressible fluid it represents stretching of B_{r} by the poloidal flow, whereas it is differently related to the flow in deeper layers in the case of compressible flows. For TG flows associated with QG columns, in particular, the third term

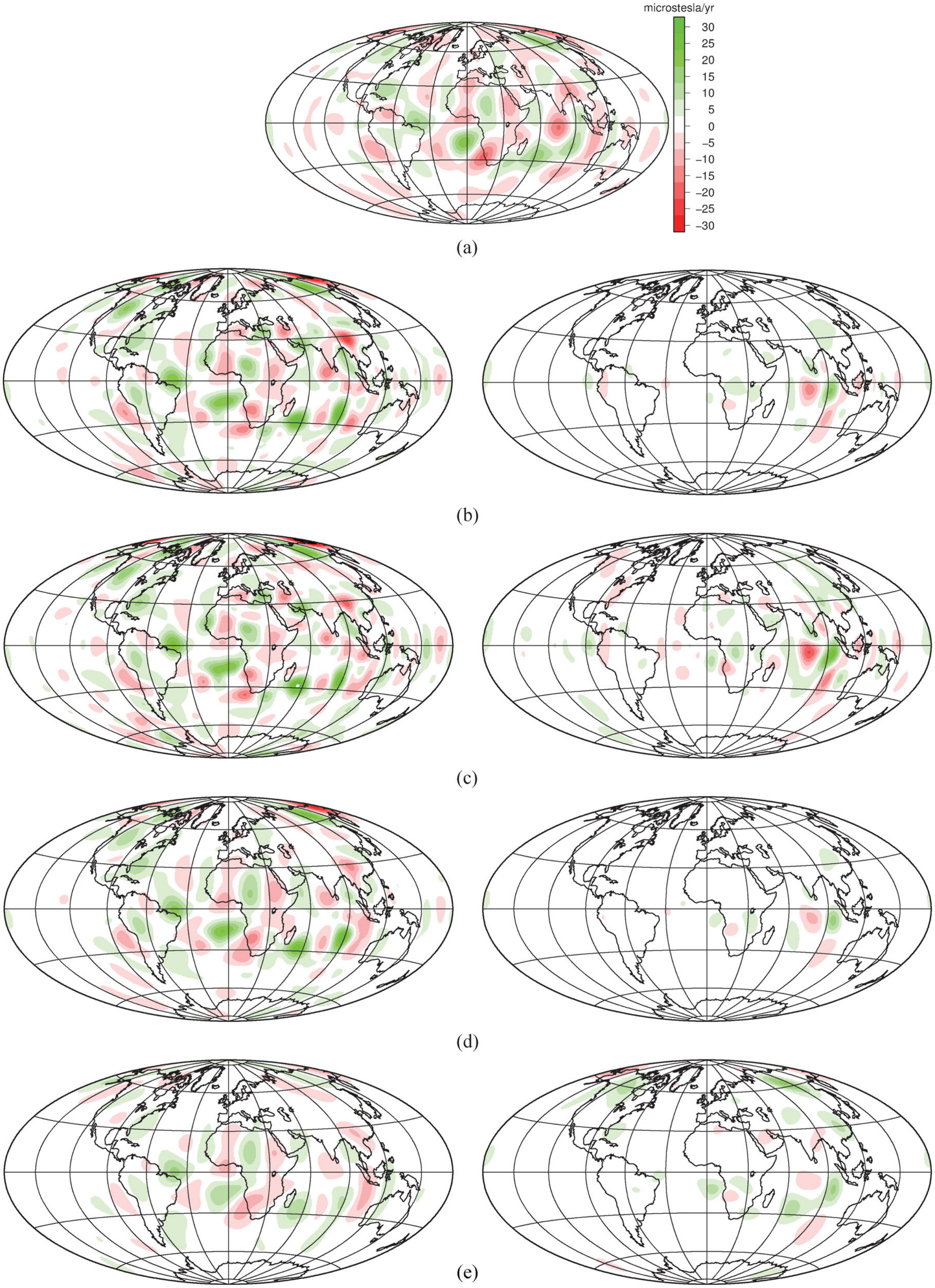

Figure 3. SV model (top) and its contributions due to advection (left) and stretching (right) of the main field by inverted flows for epoch 2005 using the *CHAOS-3* model: (a) $\dot{B}_r$; estimated contributions of $-(\vec{u}_h \cdot \nabla_h)B_r$ and $-B_r\nabla_h \cdot \vec{u}_h$ computed using (b) *TG-S*; (c) *CF-S*; (d) *TG-AS*; (e) *N-AS*.

in (1) is exactly half the value of the stretching of B_r produced by QG columns, $B_r\partial u_r/\partial r$, at each point on the CMB. Note again that the u_ϕ component in (10) does not alter this stretching, which is the same for standard and modified QG columns.

5.2 Non-uniqueness

Next we discuss the differences in localization of non-unique flow components computed using the two assumptions. We are mostly

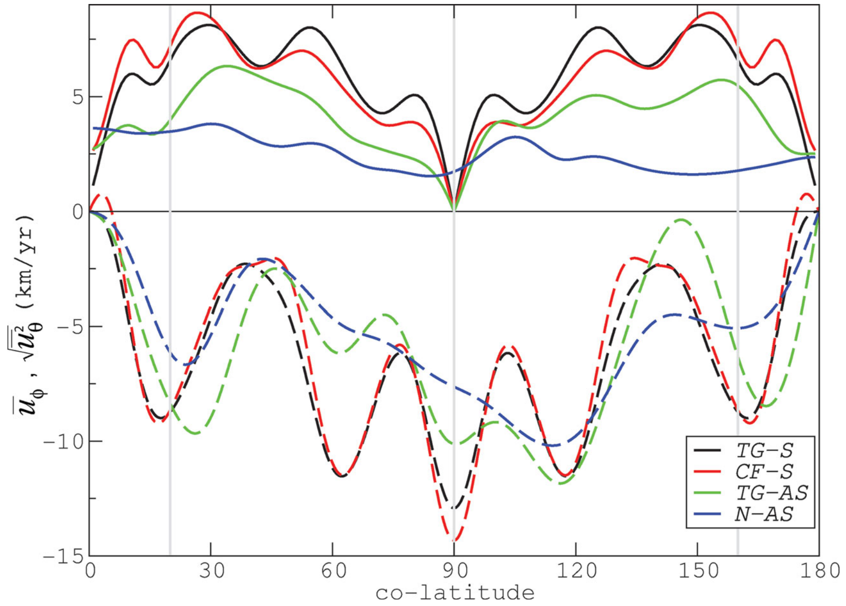

Figure 4. Zonal profiles $\overline{u}_\phi$ (dashed) and $\sqrt{\overline{u_\theta^2}}$ (solid) as a function of colatitude for the four core surface flows.

concerned about the geometrical difference between ζ_{tg} and ζ_{cf} and the resulting differences in A_{tg} and A_{cf}. We recall that an ageostrophic belt was defined in the context of a tangential magnetostrophic balance, in which case it delimits the region near the equator where the tangential Coriolis force is weak and is no longer expected to enter the main force balance. In that context, the tangential Lorentz force is the best candidate to balance the horizontal pressure gradient (Chulliat & Hulot 2000) and the critical ζ-value defining the width of the ageostrophic belt depends on the order of magnitude of horizontal electrical currents at the CMB. In the framework of a QG model, as explained above, the TG (or CF) assumption is not related to a tangential magnetostrophic balance but instead to z-invariance induced by rotational effects together with a geometrical effect due to adjustment to rigid spherical boundaries. The simultaneous weakening of Coriolis force and steepening of solid boundaries near the equator should culminate in the collapse of QG columns in that region. However, equatorial QG columns are still observed in laboratory experiments (Busse & Carrigan 1976; Cardin & Olson 1994) and numerical simulations (e.g. Olson *et al.* 1999) and there seems to be no need to define an ‘ageostrophic belt’ related to *TG-S* or *CF-S* flows.

For 1980 we find that the TG ambiguous patches cover 43.2 per cent of the CMB surface. Bloxham & Jackson (1991) reported 41 per cent for the same year, but they did not describe how this value was obtained. This small difference may possibly arise due to differences in the field models used. To our best knowledge, an algorithm to calculate the area of ambiguous patches, which we describe in detail in Appendix B, has not been reported so far.

We find minor differences between areas covered by ambiguous TG and CF patches. The global non-uniqueness reduction associated with the two assumptions is therefore comparable. In that respect, the usefulness of the two assumptions may be considered similar.

Due to the asymmetric distribution of ambiguous patches with respect to the equator (see much smaller A^s_{tg} and A^s_{cf} values compared to A_{tg} and A_{cf} in Table 1), the non-uniqueness can be reduced by an equatorial symmetric flow. The TG-S and CF-S flows in non-ambiguous regions can be used to determine the flow in ambiguous regions localized in equatorially symmetric points in the opposite hemisphere. In fact, equatorial symmetry can reduce non-uniqueness even for two points symmetric about the equator that reside in two ambiguous patches, as long as the equatorial plane projections of the two ζ-contours that cross these points are not parallel. This is analogous to non-uniqueness reduction associated with steady toroidal flows as long as the B_{r}-contours of two different snapshots are not parallel (Gubbins 1982). The equatorial plane projections of two symmetric ζ-contours will never be perfectly parallel so, hypothetically, equatorial symmetry may fully remove non-uniqueness. In practice, as with the steady toroidal flow assumption, a non-negligible angle between the two symmetric ζ-contours is required to remove non-uniqueness in pairs of symmetric points that both reside inside ambiguous patches.

Our analysis does not take into account the fact that only the large-scale B_{r} is known at the CMB, which leads to an imprecise assessment of ζ-contours. Here, for an easier comparison of the results, we followed the lines of previous studies that identified TG ambiguous regions in the space domain (Backus & LeMouël 1986; Chulliat & Hulot 2001; Chulliat 2004). As suggested by one of the reviewers, a more sensible analysis may be accomplished in the spectral domain (see Asari *et al.* 2009).

5.3 Core flows

Finally we compare the core flows resulting from different physical assumptions. These time-average flows represent persistent structures during the 14 yr time period of the *CHAOS-3* model (1997–2010). We find that in all flows the toroidal component dominates, as in most previous studies (see Finlay & Amit 2011, and references therein). Our *TG-S* flow exhibits a large eccentric gyre similar to the one found in other QG flow models that assumed TG (Pais & Jault 2008; Gillet *et al.* 2009). However, this eccentric gyre is less dominant in the *CF-S* flow, where the meridional branches bridging the high- and low-latitude westward jets are less evident. Such lack of connectivity is also seen in the flows of Schaeffer & Pais (2011) that assumed CF for the equatorially symmetric part of the flow. This difference suggests that the inference of a large eccentric gyre might not be compatible with incompressibility. The Atlantic/Pacific dichotomy in core flow activity is also less striking in the CF flow. The corresponding Atlantic/Pacific dichotomy in SV has been identified in the present field (Hulot *et al.* 2002; Holme *et al.* 2011) and possibly in palaeomagnetic records (Christensen & Olson 2003; Gubbins 2003), suggesting that the influence of a heterogeneous lower mantle may drive stronger flows in the Atlantic. Amit & Christensen (2008) argued that accounting for magnetic diffusion yields relatively stronger core flows in the Pacific. Overall, caution should be taken when inferring hemispheric dichotomy in core flow directly from the observed hemispheric dichotomy in geomagnetic SV.

All four flow maps exhibit some flow crossing the tangent cylinder. However, a more appropriate implementation of the CF assumption inside the tangent cylinder is needed in order to better resolve the flow there (for further discussion on this subject see Pais & Jault 2008). Also, Schaeffer & Pais (2011) showed that favouring zonation decouples the flow inside and outside the tangent cylinder.

The upwelling pattern characteristic of QG columns, given by (14) and (15) for TG and CF, respectively, is consistent with surface divergence of columnar flow going from higher to lower latitudes (contracted columns) and surface convergence of columnar flow going from lower to higher latitudes (stretched columns). It is at the equator, where QG columns are most contracted or stretched, that largest values of the tangential divergence occur, as observed in Figs 2(a)–(b) where a low-latitude QG column South of India is clearly seen. Note that in order to resolve such a column with a lengthscale of about $R\pi/6$, flow features of degree $\ell = 12, 13$ should be undamped. The overwhelming concentration of tangential divergence structures at the equator is in agreement with previous upwelling maps derived from TG flows (Gire & LeMouël 1990; Bloxham & Jackson 1991). These intense equatorial upwelling/downwelling structures emerge due to the $\tan\theta$ dependence in (14) and (15), as noted by Olson *et al.* (2002). A different upwelling/downwelling relation with the toroidal flow, characterized by the presence of ascending/descending flows at the centre of vortices and thus promoting helicity, is found in numerical dynamo models (e.g. Olson *et al.* 1999, 2002). The helical geostrophic assumption of Amit & Olson (2004) results in equatorial upwelling/downwelling structures due to the TG assumption but also some mid- and high-latitudes tangential divergence features associated with their helical flow assumption.

Next we compare the upwelling distribution and the poloidal/toroidal RMS velocity ratio in the *TG-S* and *CF-S* flows. The tangential divergence depends only on the poloidal scalar ($\nabla_{\rm h} \cdot \vec{u}_{\rm h} = \nabla_{\rm h}^2 \mathcal{P}$), but both poloidal and toroidal scalars contribute to u_θ on the right-hand side of (14) and (15). We therefore should not expect a simple increase of the relative value of the poloidal scalar by a factor 2 when comparing flows inverted with the TG and CF assumptions. Moreover, the two scalar potentials contribute differently for the advection and stretching of $B_{\rm r}$ in (1). Increasing the relative importance of $\mathcal{P}$ increases the relative importance of the stretching term which requires, with the same SV to be explained, that the contribution of the advection term recedes. However, the SV 'data' is mainly explained by the advection term in most of the core surface (see Fig. 3), and the stretching term is only moderately larger in *CF-S*. The flow adjusts so that condition (15) is verified with only a moderate increase of $\nabla_{\rm h} \cdot \vec{u}_{\rm h}$ and of the poloidal scalar $\mathcal{P}$, as confirmed by the computed increase by a factor of 1.3 in the ratio $\langle \vec{u}_{\rm pol} \rangle / \langle \vec{u}_{\rm tor} \rangle$ (Table 2). This is particularly clear in the two nearly meridional branches of the eccentric jet, where relatively high u_θ values occur. Because the SV 'data' is not compatible with doubling of $\nabla_{\rm h} \cdot \vec{u}_{\rm h}$, the meridional *CF-S* flow decreases with respect to the meridional *TG-S* flow to verify condition (15). As a result, these meridional branches of the eccentric jet are less clearly outlined in *CF-S* than in *TG-S*. The weaker $\sqrt{\overline{u_\theta^2}}$ and slightly stronger $\overline{u}_\phi$ in low- and mid-latitudes of *CF-S* (see Fig. 4) may suggest a spiralling of the flow in the equatorial plane instead of a closed jet, as found in a core flow inversion of geomagnetic SV which relies on the relations between the field and the flow in a 3-D self-consistent numerical dynamo simulation (Aubert 2013). There are nevertheless regions on the core surface where the stretching effect in *CF-S* is significantly larger with respect to *TG-S*, mainly the equatorial region below India and Indonesia (Fig. 3). In addition, new tangential divergence features emerge along the equatorial branch of the jet in the *CF-S* flow (Fig. 2b), suggesting that the jet may form as the superposition of adjoining QG columns. Overall, it could be that the poloidal *CF-S* flow magnitude does not increase with respect to its *TG-S* counterpart by the expected factor 2 because the regions where there can be upwelling are well constrained by the SV (Beggan & Whaler 2008).

We gradually decrease the number of flow constraints in the inversion, going from equatorially symmetric *TG-S* and *CF-S* flows to *TG-AS* and further *N-AS* flows in which equatorial symmetry is not imposed. Fewer constraints blur most small scale flow features to the point that the large scale regularization effect dominates (Fig. 2d). When removing the equatorial symmetry constraint in *TG-AS*, the increased effect of ℓ^3 regularization is seen in the larger scale flow structures (Fig. 2c) and in the decrease of RMS velocities (Table 2). The flow signature of the rim of the tangent cylinder under the Pacific Hemisphere gets blurred, especially in the Southern Hemisphere. Both the upwelling pattern and the westward drift under the Atlantic Ocean are nearly symmetric in the equatorial region (Figs 2c and 4). The columnar behaviour is clearly disturbed at higher latitudes, for example, the southern counterpart of the anticyclonic vortex below North America and the northern counterpart of the anticyclone vortex below south of Southern Africa, both become very dim.

When the TG constraint is removed in flow *N-AS*, more antisymmetric features emerge in the equatorial region (Fig. 2d). The global flow is displaced southwards (westward drift and upwelling pattern below the Indian Ocean, see Figs 2d and 4), with some flow crossing the geographical equator below the Atlantic Hemisphere. We remark, in particular, the presence of upwelling/downwelling structures below the Indian Ocean, a recurrent feature in previous flow inversions (Gire & LeMouël 1990; Amit & Olson 2006) using various assumptions, and in all flows computed here. This supports robustness of this poloidal flow feature, which may be viewed as geomagnetic evidence for whole core convection, in contrast to recent arguments in favour of stratification at the top of Earth's core (Helffrich & Kaneshima 2010; Pozzo *et al.* 2012). Fig. 2(d) also shows high-latitudes upwelling/downwelling structures that do not appear in the *TG-S* and *CF-S* flows. The most important upwellings are localized next to the Pacific rim of the tangent cylinder in the Northern Hemisphere where *TG-S* and *CF-S* flows show a very strong, almost azimuthal jet. Because both $B_{\rm r}$ and $\dot{B}_{\rm r}$ show intense features in this region for the studied period (Finlay *et al.* 2012), it seems that while the *TG-S* and *CF-S* flows explain the strong observed SV in this region through advection of $B_{\rm r}$ by the strong azimuthal jet, the SV could also be explained through stretching of $B_{\rm r}$ by upwelling (Beggan & Whaler 2008). In fact, as Fig. 3(e) confirms, the SV below the Northern Pacific Ocean may have an important contribution from stretching of the geomagnetic field. If that is the case, QG columnar flow contribution could be dismissed there.

6 CONCLUSIONS

The main findings of this paper are:

(1) Ambiguous patches associated with CF are defined by contours of $\zeta_{\rm cf} = B_{\rm r}/\cos^2\theta$ that do not cross the equator. The difference between $\zeta_{\rm tg}$ and $\zeta_{\rm cf}$ lies essentially in a latitude-dependent amplification of $\zeta_{\rm cf}$.

(2) The global non-uniqueness reduction associated with TG and CF is comparable. Due to the equatorial asymmetry of ambiguous patches, non-uniqueness can significantly be reduced if flow in non-ambiguous patches can be used to constrain the flow in the opposite hemisphere, assuming a columnar structure. Such a scenario of columnar convection is supported by theoretical, numerical and experimental studies.

(3) Flows inverted using TG exhibit an eccentric gyre and a strong Atlantic/Pacific flow dichotomy, but in CF flows the gyre and the hemispheric dichotomy are less striking, possibly indicating that an eccentric columnar gyre as the one computed using TG is violating the incompressibility condition.

(4) Both TG and CF upwelling patterns are overwhelmingly concentrated at the equatorial region along meridional flow branches.

(5) The magnitude of CF upwelling is larger than its TG counterpart, but by less than the theoretically expected factor 2, demonstrating the dominance of magnetic field advection over stretching in the SV.

(6) Robust upwelling features, for example, below the Indian Ocean, may suggest whole core convection.

The modified QG model of Schaeffer & Cardin (2005), in conjunction with the surface condition CF (and not TG), consistently enforces conservation of mass in both the volume and surface flows. The importance of a proper downward projection of inverted core surface flows to reconstruct QG columns in the fluid core volume should not be underestimated, if these columns are to be used in dynamical studies of the core. This is the case in data assimilation studies which hindcast/forecast the geomagnetic field (e.g. Canet *et al.* 2009), kinematic dynamos which assess the ability of QG flows to sustain the geodynamo (e.g. Schaeffer & Cardin 2006) or thermal convection models which may determine the thermodynamic evolution of the core. As we revise here, QG columns recovered from an equatorially symmetric TG flow do not satisfy incompressibility. Also, incompressible QG columns cannot be recovered from an equatorially symmetric TG flow simply by doubling the poloidal content of the surface flow; the CF assumption has to be explicitly used in the inversion.

By optimizing physical assumptions and understanding their limitations, inferences from geomagnetic field data may provide more reliable images of the flow at the top of the core, and perhaps even allow a glimpse into deep core dynamics (Gillet *et al.* 2010; Aubert & Fournier 2011). In the coming years, the SWARM magnetic satellites constellation (Friis-Christensen *et al.* 2006) will continue to provide high-quality data for geomagnetic field models. Applying the theoretical and numerical tools proposed in this study to SWARM-derived geomagnetic field and SV models will advance the understanding of the dynamics in Earth's outer core.

ACKNOWLEDGEMENTS

This study was supported by the Centre National d'Études Spatiales (CNES), Fundação para a Ciência e Tecnologia (FCT: PTDC/CTE-GIX/119967/2010) and FEDER through the project COMPETE (FCOMP-01-0124-FEDER-019978). We are grateful to two anonymous reviewers and Richard Holme for constructive suggestions that significantly improved the manuscript.

REFERENCES

Amit, H. & Christensen, U., 2008. Accounting for magnetic diffusion in core flow inversions from geomagnetic secular variation, *Geophys. J. Int.,* **175,** 913–924.

Amit, H. & Olson, P., 2004. Helical core flow from geomagnetic secular variation, *Phys. Earth planet. Inter.,* **147,** 1–25.

Amit, H. & Olson, P., 2006. Time-average and time-dependent parts of core flow, *Phys. Earth planet. Inter.,* **155,** 120–139.

Asari, S. & Lesur, V., 2011. Radial vorticity constraint in core flow modeling, *J. geophys. Res.,* **116,** B11101, doi:10.1029/2011JB008267.

Asari, S., Shimizu, H. & Utada, H., 2009. Robust and less robust features in the tangential geostrophy core flows, *Geophys. J. Int.,* **178,** 678–692.

Aubert, J., 2013. Flow throughout the Earth's core inverted from geomagnetic observations and numerical dynamo models, *Geophys. J. Int.,* **192,** 537–556.

Aubert, J. & Fournier, A., 2011. Inferring internal properties of Earth's core dynamics and their evolution from surface observations and a numerical geodynamo model, *Nonlinear Proc. Geoph.,* **18,** 657–674.

Backus, G., 1968. Kinematics of geomagnetic secular variation in a perfectly conducting core, *Phil. Trans. R. Soc. Lond. A,* **263,** 239–266.

Backus, G. & LeMouël, J.-L., 1986. The region on the core mantle boundary where a geostrophic velocity field can be determined from frozen flux magnetic data, *Geophys. J. R. astron. Soc.,* **85,** 617–628.

Beggan, C. & Whaler, K., 2008. Core flow modelling assumptions, *Phys. Earth planet. Inter.,* **167,** 217–222.

Bloxham, J. & Jackson, A., 1991. Fluid flow near the surface of the Earth's outer core, *Rev. Geophys.,* **29,** 97–120.

Busse, F., 1970. Thermal instabilities in rapidly rotating systems, *J. Fluid Mech.,* **44,** 441–460.

Busse, F. & Carrigan, C.R., 1976. Laboratory simulation of thermal convection in rotating planets and stars, *Science,* **191,** 81–83.

Canet, E., Fournier, A. & Jault, D., 2009. Forward and adjoint quasi-geostrophic models of the geomagnetic secular variation, *J. geophys. Res.,* **114,** doi:10.1029/2008JB006189.

Cardin, P. & Olson, P., 1994. Chaotic thermal convection in a rapidly rotating spherical shell: consequences for flow in the outer core, *Phys. Earth planet. Inter.,* **82,** 235–259.

Christensen, U. & Olson, P., 2003. Secular variation in numerical geodynamo models with lateral variations of boundary heat flow, *Phys. Earth planet. Inter.,* **138,** 39–54.

Christensen, U. & Wicht, J., 2007. Numerical dynamo simulations, in *Treatise on Geophysics*. Vol. 8, ed. Olson, P., Elsevier Science, Amsterdam.

Chulliat, A., 2004. Geomagnetic secular variation generated by a tangentially geostrophic flow under the frozen-flux assumption—II. Sufficient conditions, *Geophys. J. Int.,* **157,** 537–552.

Chulliat, A. & Hulot, G., 2000. Local computation of the geostrophic pressure at the top of the core, *Phys. Earth planet. Inter.,* **117,** 309–328.

Chulliat, A. & Hulot, G., 2001. Geomagnetic secular variation generated by a tangentially geostrophic flow under the frozen-flux assumption—I. Necessary conditions, *Geophys. J. Int.,* **147,** 237–246.

Eymin, C. & Hulot, G., 2005. On surface core flows inferred from satellite magnetic data, *Phys. Earth planet. Inter.,* **152,** 200–220.

Finlay, C.C. & Amit, H., 2011. On flow magnitude and field-flow alignment at Earth's core surface, *Geophys. J. Int.,* **186,** 175–192.

Finlay, C.C., Dumberry, M., Chulliat, A. & Pais, M.A., 2010. Short timescale core dynamics: theory and observations, *Space Sci. Rev.,* **155,** 177–218.

Finlay, C., Jackson, A., Gillet, N. & Olsen, N., 2012. Core surface magnetic field evolution 2000–2010, *Geophys. J. Int.,* **189,** 761–781.

Friis-Christensen, E., Lühr, H. & Hulot, G., 2006. Swarm: a constellation to study the Earth's magnetic field, *Earth Planets Space,* **58,** 351–358.

Gillet, N., Jault, D., Canet, E. & Fournier, A., 2010. Fast torsional oscillations and strong magnetic field within the Earth's core, *Nature,* **465,** 74–77.

Gillet, N., Pais, M.A. & Jault, D., 2009. Ensemble inversion of time-dependent core flow models, *Geochem. Geophys. Geosyst.,* **10,** doi:10.1029/2008GC002290.

Gire, C. & LeMouël, J.-L., 1990. Tangentially-geostrophic flow at the core-mantle boundary compatible with the observed geomagnetic secular variation: the large-scale component of the flow, *Phys. Earth planet. Inter.,* **59,** 259–287.

Gubbins, D., 1982. Finding core motions from magnetic observations, *Phil. Trans. R. Soc. Lond. A,* **306,** 249–256.

Gubbins, D., 2003. Thermal core-mantle interactions: theory and observations, in *Earth's Core: Dynamics, Structure and Rotation,* AGU Geodynamics Series, eds Dehant, V., Creager, K., Karato, S. & Zatman, S., American Geophysical Union.

Helffrich, G. & Kaneshima, S., 2010. Outer-core compositional stratification from observed core wave speed profiles, *Nature,* **468,** 807–810.

Hills, R., 1979. Convection in the Earth's mantle due to viscous shear at the core-mantle interface and due to large-scale buoyancy, *PhD thesis,* New Mexico State University.

Holme, R., 2007. Large-scale flow in the core, in *Treatise on Geophysics,* Vol. **8,** ed. Olson, P., Elsevier Science, Amsterdam.

Holme, R. & Whaler, K., 2001. Steady core flow in an azimuthally drifting reference frame, *Geophys. J. Int.,* **145,** 560–569.

Holme, R., Olsen, N. & Bairstow, F., 2011. Mapping geomagnetic secular variation at the coremantle boundary, *Geophys. J. Int.,* **186,** 521–528.

Hulot, G., Eymin, C., Langlais, B., Mandea, M. & Olsen, N., 2002. Small-scale structure of the geodynamo inferred from Oersted and Magsat satellite data, *Nature,* **416,** 620–623.

Jackson, A., 1997. Time-dependency of tangentially geostrophic core surface motions, *Phys. Earth planet. Inter.,* **103,** 293–311.

Jackson, A., Bloxham, J. & Gubbins, D., 1993. Time-dependent flow at the core surface and conservation of angular momentum in the coupled core-mantle system, in *Dynamics of Earth's Deep Interior and Earth Rotation*. Vol. **12,** eds LeMouël, J.-L., Smylie, D. & Herring, T., Geophysical Monograph 72 IUGG, IUGG/AGU, Washington, DC, USA.

Jackson, A., Jonkers, A. & Walker, M., 2000. Four centuries of geomagnetic secular variation from historical records, *Phil. Trans. R. Soc. Lond., A,* **358,** 957–990.

Jault, D., Gire, C. & LeMouël, J.-L., 1988. Westward drift, core motions and exchanges of angular momentum between core and mantle, *Nature,* **333,** 353–356.

LeMouël, J.-L., 1984. Outer core geostrophic flow and secular variation of Earth's magnetic field, *Nature,* **311,** 734–735.

Lesur, V., Wardinski, I., Hamoudi, M. & Rother, M., 2010. The second generation of the GFZ Reference Internal Magnetic Model: GRIMM-2, *Earth Planets Space,* **62,** 765–773.

Olsen, N. & Mandea, M., 2008. Rapidly changing flows in the Earth's core, *Nat. Geosci.,* **1,** 390–394.

Olson, P., Christensen, U. & Glatzmaier, G., 1999. Numerical modeling of the geodynamo: mechanisms of field generation and equilibration, *J. geophys. Res.,* **104,** 10 383–10 404.

Olson, P., Sumita, I. & Aurnou, J., 2002. Diffusive magnetic images of upwelling patterns in the core, *J. geophys. Res.,* **107,** doi:10.1029/2001jb000384.

Olsen, N., Mandea, M., Sabaka, T. & Tøffner-Clausen, L., 2010. The CHAOS-3 geomagnetic field model and candidates for the 11th generation IGRF, *Earth Planets Space,* **62,** 719–727.

Pais, A. & Hulot, G., 2000. Length of day decade variations, torsional oscillations and inner core superrotation:evidence from recovered core surface zonal flows, *Phys. Earth planet. Inter.,* **118,** 291–316.

Pais, M.A. & Jault, D., 2008. Quasi-geostrophic flows responsible for the secular variation of the Earth's magnetic field, *Geophys. J. Int.,* **173,** 421–443.

Pedlosky, J., 1987. *Geophysical Fluid Dynamics*. Springer-Verlag, New York, USA.

Pozzo, M., Davies, C., Gubbins, D. & Alfè, D., 2012. Thermal and electrical conductivity of iron at Earth's core conditions, *Nature,* **485,** 355–358.

Press, W., Flannery, B., Teukolsky, S. & Vetterling, W., 1989. *Numerical recipes in Fortran 77*. Cambridge University Press, Cambridge, UK.

Roberts, P. & Scott, S., 1965. On analysis of the secular variation. 1. A hydromagnetic constraint: theory, *J. Geomagn. Geoelectr.,* **17,** 137–151.

Schaeffer, N. & Cardin, P., 2005. Quasigeostrophic model of the instabilities of the Stewartson layer in flat and depth-varying containers, *Phys. Fluids,* **17,** 104111, doi:10.1063/1.2073547.

Schaeffer, N. & Cardin, P., 2006. Quasigeostrophic kinematic dynamos at low magnetic Prandtl numbers, *Earth planet. Sci. Lett.,* **245,** 595–604.

Schaeffer, N. & Pais, M.A., 2011. On symmetry and anisotropy of Earth-core flows, *Geophys. Res. Lett.,* **38,** L10309, doi:10.1029/2011GL046888.

Schubert, G., Turcotte, D. & Olson, P., 2001. *Mantle convection in the Earth and planets*. Cambridge University Press, Cambridge, UK.

Whaler, K., 1980. Does the whole of Earth's core convect? *Nature,* **287,** 528–530.

APPENDIX A: NON-UNIQUENESS OF TANGENTIAL GEOSTROPHY VERSUS COLUMNAR FLOW

The non-uniqueness can be shown by considering the radial induction equation at the top of the core in the frozen-flux approximation (1). For TG, it is useful to rewrite (1) as

$$\frac{\partial B_\mathrm{r}}{\partial t} + \nabla_\mathrm{h} \cdot \left(\frac{B_\mathrm{r}}{\cos\theta} \cos\theta \vec{u}_\mathrm{h} \right) = 0, \tag{A1}$$

which can be further rewritten as

$$\frac{\partial B_\mathrm{r}}{\partial t} + \frac{B_\mathrm{r}}{\cos\theta} \nabla_\mathrm{h} \cdot (\vec{u}_\mathrm{h} \cos\theta) + \cos\theta \vec{u}_\mathrm{h} \cdot \nabla \left(\frac{B_\mathrm{r}}{\cos\theta} \right) = 0. \tag{A2}$$

For TG flows (13) holds, so the second term in (A2) vanishes. The TG flows that do not produce SV are therefore parallel to contours of $\zeta_\mathrm{tg} = B_\mathrm{r}/\cos\theta$.

Similarly, for CF we write

$$\frac{\partial B_\mathrm{r}}{\partial t} + \nabla_\mathrm{h} \cdot \left(\frac{B_\mathrm{r}}{\cos^2\theta} \cos^2\theta \vec{u}_\mathrm{h} \right) = 0, \tag{A3}$$

$$\frac{\partial B_\mathrm{r}}{\partial t} + \frac{B_\mathrm{r}}{\cos^2\theta} \nabla_\mathrm{h} \cdot \left(\vec{u}_\mathrm{h} \cos^2\theta \right) + \cos^2\theta \vec{u}_\mathrm{h} \cdot \nabla \left(\frac{B_\mathrm{r}}{\cos^2\theta} \right) = 0. \tag{A4}$$

For CF flows (16) holds, so the second term in (A4) vanishes. The CF flows that do not produce SV are therefore parallel to contours of $\zeta_\mathrm{cf} = B_\mathrm{r}/\cos^2\theta$.

APPENDIX B: AN ALGORITHM TO CALCULATE THE AREA OF AMBIGUOUS PATCHES

Let ζ be the streamline of an invisible flow (either $B_\mathrm{r}/\cos\theta$ for TG, or $B_\mathrm{r}/\cos^2\theta$ for CF). The goal is to decide for every longitude/colatitude gridpoint (ϕ_0, θ_0) on the CMB whether it belongs to an ambiguous patch or not. The algorithm follows the $\zeta(\phi_0, \theta_0)$ contour until reaching either an equatorial nodal point or the initial point (ϕ_0, θ_0). The algorithm is as follows:

(1) Determine the direction tangent to the ζ contour at (ϕ_i, θ_i). This direction vector $\vec{d}$ is given by

$$\vec{d} = \hat{r} \times \nabla_\mathrm{h}\zeta = \frac{1}{R}\frac{\partial\zeta}{\partial\theta}\hat{\phi} - \frac{1}{R\sin\theta}\frac{\partial\zeta}{\partial\phi}\hat{\theta}. \tag{B1}$$

The vector $\vec{d}$ is calculated analytically based on the Gauss coefficients of the field model g_l^m and h_l^m. For TG, (B1) becomes

$$d_\phi = \frac{1}{R\cos\theta}\sum_{\ell=1}^{\ell_{\max}}\sum_{m=0}^{\ell} S_\ell^m\,(\ell+1)\left(\frac{a}{R}\right)^{\ell+2}\left(m\cot\theta\, P_\ell^m + P_\ell^{m+1}\right.$$

$$\left. + \tan\theta\, P_\ell^m\right)\left(g_\ell^m\cos(m\phi) + h_\ell^m\sin(m\phi)\right) \qquad \text{(B2)}$$

$$d_\theta = -\frac{1}{R\cos\theta\sin\theta}\sum_{\ell=1}^{\ell_{\max}}\sum_{m=0}^{\ell} S_\ell^m\,(\ell+1)\left(\frac{a}{R}\right)^{\ell+2} P_\ell^m$$

$$\cdot m\left(-g_\ell^m\sin(m\phi) + h_\ell^m\cos(m\phi)\right) \qquad \text{(B3)}$$

and for CF, (B1) becomes

$$d_\phi = \frac{1}{R\cos^2\theta}\sum_{\ell=1}^{\ell_{\max}}\sum_{m=0}^{\ell} S_\ell^m\,(\ell+1)\left(\frac{a}{R}\right)^{\ell+2}\left(m\cot\theta\, P_\ell^m + P_\ell^{m+1}\right.$$

$$\left. + 2\tan\theta\, P_\ell^m\right)\cdot\left(g_\ell^m\cos(m\phi) + h_\ell^m\sin(m\phi)\right) \qquad \text{(B4)}$$

$$d_\theta = -\frac{1}{R\cos^2\theta\sin\theta}\sum_{\ell=1}^{\ell_{\max}}\sum_{m=0}^{\ell} S_\ell^m\,(\ell+1)\left(\frac{a}{R}\right)^{\ell+2} P_\ell^m$$

$$\cdot m\left(-g_\ell^m\sin(m\phi) + h_\ell^m\cos(m\phi)\right) \qquad \text{(B5)}$$

In (B2)–(B5) ℓ and m are the spherical harmonics degree and order, $\ell_{\max}$ is the truncation degree, a and R are Earth's surface and the CMB radii, S_ℓ^m is the Schmidt semi-normalization factor and P_l^m is the associated Legendre function. The latitudinal derivative of P_l^m was taken from the recurrence relation for associated Legendre polynomials (e.g. Schubert *et al.* 2001):

$$\frac{\mathrm{d}P_\ell^m}{\mathrm{d}\theta} = m\cot\theta\, P_\ell^m + P_\ell^{m+1} = -m\cot\theta\, P_\ell^m - (m+\ell)$$

$$\times\,(\ell - m + 1)\, P_\ell^{m-1} \qquad \text{(B6)}$$

where the second equality is used for $m = \ell$. Since only direction matters here, we normalize $\vec{d}$:

$$\hat{d} = \frac{\vec{d}}{|\vec{d}|} \qquad \text{(B7)}$$

(2) Use the unit direction vector $\hat{d}$ to forward iterate along ζ (in both directions). For decent numerical accuracy we used a two-step Adams Bashforth scheme (Press *et al.* 1989):

$$\phi_{i+2}^{+} = \phi_{i+1} + \frac{3}{2}d_{\phi\,i+1}\frac{\delta}{\sin\theta_i} - \frac{1}{2}d_{\phi\,i}\frac{\delta}{\sin\theta_i},$$

$$\theta_{i+2}^{+} = \theta_{i+1} + \frac{3}{2}d_{\theta\,i+1}\delta - \frac{1}{2}d_{\theta\,i}\delta, \qquad \text{(B8)}$$

$$\phi_{i+2}^{-} = \phi_{i+1} - \frac{3}{2}d_{\phi\,i+1}\frac{\delta}{\sin\theta_i} + \frac{1}{2}d_{\phi\,i}\frac{\delta}{\sin\theta_i},$$

$$\theta_{i+2}^{-} = \theta_{i+1} - \frac{3}{2}d_{\theta\,i+1}\delta + \frac{1}{2}d_{\theta\,i}\delta, \qquad \text{(B9)}$$

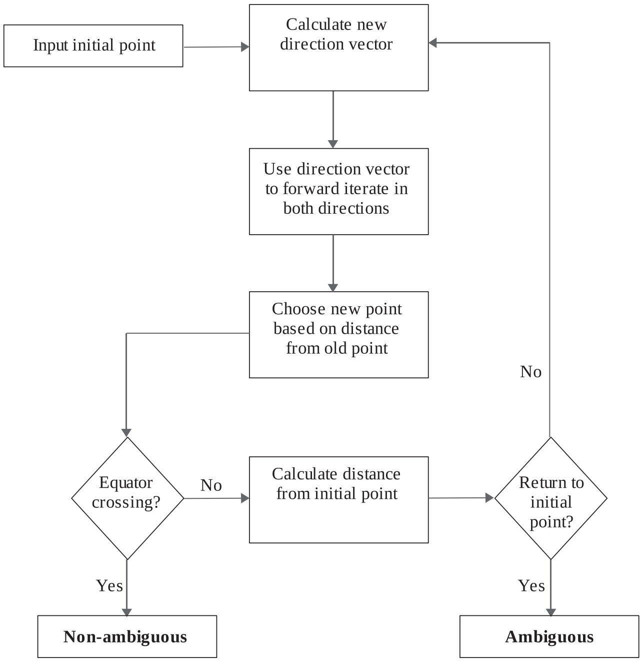

Figure B1. Flowchart of the algorithm for determining whether a gridpoint is ambiguous or not.

where the subscript i denotes the iteration, the superscripts + and − represent the two possible directions of iteration along ζ and δ is a small spatial step. Note that the new point (ϕ_{i+2}, θ_{i+2}) is not part of the initial grid. Also note the factor $\sin\theta$ dividing d_ϕ which accounts for the latitudinal dependence of a surface increment in spherical coordinates.

(3) Choose $(\phi_{i+2}, \theta_{i+2})^{+}$ or $(\phi_{i+2}, \theta_{i+2})^{-}$ depending on which point is further from the point of the previous iteration (ϕ_i, θ_i) in order to move monotonously rather than back and forth.

(4) Equator crossing? If $\theta_{i+2} > \pi/2$ and $\theta_0 < \pi/2$ or $\theta_{i+2} < \pi/2$ and $\theta_0 > \pi/2$ then the initial gridpoint (ϕ_0, θ_0) is 'non-ambiguous'.

(5) Return to initial point? If (ϕ_{i+2}, θ_{i+2}) is very close to the initial grid point (ϕ_0, θ_0), then (ϕ_0, θ_0) is 'ambiguous'. This part of the algorithm requires defining a small distance threshold for identifying the return point.

(6) If both conditions (4) and (5) are not yet satisfied, return to step 1 for a new iteration using point (ϕ_{i+2}, θ_{i+2}).

A flowchart of the algorithm is shown in Fig. B1.

The algorithm is repeated for all CMB gridpoints. We used a regular 5° × 5° grid in ϕ and θ. Once each gridpoint is determined ambiguous or not, the relative area of ambiguous patches is integrated over the CMB surface. The relative areas are rather insensitive to the spatial resolution. Using a finer 2.5° × 2.5° grid, differences of ∼0.2 per cent in the relative areas are found.